## Main Manuscript for

# Iron mineral dissolution during permafrost thaw releases associated organic carbon

**Monique S. Patzner[1], Carsten W. Mueller[2], Miroslava Malusova[1], Verena Nikeleit[1], Thomas Scholten[3], Carmen Hoeschen[2], James M. Byrne[1], Thomas Borch[4], Andreas Kappler[1] & Casey Bryce[1]***

[1] Geomicrobiology, Center for Applied Geosciences, University of Tuebingen, Tuebingen, Germany.

[2] Chair of Soil Science, Technical University Muenchen, Freising, Germany.

[3] Chair of Soil Science and Geomorphology, University of Tuebingen, 72070 Germany.

[4] Department of Soil & Crop Sciences and Department of Chemistry, Colorado State University, Fort Collins, US.

***Corresponding Author:** Casey Bryce **Email:** casey.bryce@uni-tuebingen.de

**Classification**

PHYSICAL SCIENCES: Environmental Sciences.

**Keywords**

iron carbon associations, iron reduction, Abisko, Arctic, peatland

**Author Contributions**

The original hypothesis was formulated by C.B and A.K. M.P, C.B and A.K designed the project, interpreted the data and wrote the manuscript. M.P, C.B and M.M collected the samples. M.P gathered the data presented in the main text. Supporting information from the 2017 campaign was collected by V.N, M.M and C.B. T.B conducted the synchrotron analysis and contributed to the data analysis and interpretation. C. H. and C.W.M, together with M.P, collected, analyzed and interpreted the nanoSIMS data. J.B and M.P conducted the SEM analyses. T.S contributed to project design and data interpretation. All authors contributed to the preparation of the manuscript.

**This PDF file includes:**

Main Text

Figures 1 to 4

Figures S1 to S9

Tables S1

## Abstract

The release of vast amounts of organic carbon during thawing of high-latitude permafrost is an emerging issue of global concern, yet it is unclear what controls the amount of this released carbon that will be subsequently metabolized and emitted as greenhouse gases. It has been shown that reactive soil minerals, specifically iron (oxyhydr)oxides, can trap approximately 20% of total organic carbon in soils overlying intact permafrost (1), and may limit carbon mobilization and degradation as is observed in other environments. However, the stability of iron-bearing minerals and thus their capacity to prevent carbon mobilization during permafrost thaw is entirely unknown. We have followed the dynamic interactions between iron and carbon across a thaw gradient in Abisko (Sweden), where wetlands are expanding rapidly due to permafrost thaw. Using both bulk (selective extractions, EXAFS) and nanoscale analysis (correlative SEM and nanoSIMS), we found that a maximum of 19.4±0.7% of the total soil organic carbon is associated with reactive iron minerals in palsas underlain by intact permafrost. However, the soil becomes water-logged and oxygen limited when palsas collapse, resulting in reducing conditions, an increase in abundance of Fe(III)-reducing bacteria, and a mobilization of both iron and carbon along the thaw gradient. Our results show that waterlogging and anoxia associated with permafrost thaw effectively destroys this “rusty carbon sink” (2) in permafrost soils.


## Significance Statement

There is significant concern that warming-induced permafrost collapse will release yet more greenhouse gases like $CO_2$ and $CH_4$. It has been shown that reactive iron minerals in soils can protect carbon from degradation in intact permafrost regions, providing a so-called “rusty carbon sink” and limiting emissions. However, our results demonstrate that reactive iron minerals only stabilize carbon when permafrost is intact. When permafrost thaws, microbially-driven mineral dissolution releases trapped carbon. We show that the “rusty carbon sink” is vulnerable to thaw-induced changes in redox state, and identify an over-looked source of

organic carbon to thaw lakes and wetlands in permafrost regions. Release of mineral-associated carbon may have consequences for greenhouse gas emissions that are unaccounted for in current predictions.

## Main Text

### Introduction

Permafrost soils store almost twice as much carbon as is currently present in the atmosphere (3, 4), which is at risk of being released as greenhouse gases (i.e., $CO_2$ or $CH_4$) during thawing. Release of greenhouse gases from permafrost soils provides a feedback which will likely lead to faster warming than predicted from anthropogenic activities alone (5). This is especially concerning considering that high latitude regions are experiencing significantly higher rates of warming than the global average (0.6°C per decade in Northern Hemisphere, 1.35°C per decade in the Arctic specifically) (6, 7). However, the extent of greenhouse gas emissions from thawing permafrost remains unpredictable due to knowledge gaps related to controls on the fate of carbon in permafrost soils. Indeed, it has been suggested that the permafrost-carbon feedback is the most important carbon-cycle feedback missing from climate models and one of the greatest uncertainties in future climate predictions (8).

The mobility, lability and bioavailability of organic carbon in the environment is determined by a number of interconnected physico-biogeochemical parameters and processes. One such parameter is the presence of reactive iron minerals (defined here as iron minerals that are reductively dissolved by the chemical reductant sodium dithionite, e.g. ferrihydrite or goethite). These minerals are known to sorb and co-precipitate organic carbon (9) and are thought to significantly influence long-term carbon storage in numerous environments (10-13). For example, approximately 20% of total organic carbon in marine sediments is associated with such reactive iron minerals (12).

However, the inventory of reactive iron minerals in natural systems is very dynamic as they precipitate and dissolve as a response to changing redox conditions. When mineral dissolution occurs, carbon mobilization, increased carbon lability/bioavailability and increased gaseous carbon loss as $CO_2$ and $CH_4$ follows (catalyzed by heterotrophic and methanogenic microorganisms) (14-18). Despite the importance of iron minerals for carbon storage, we have little empirical understanding of the presence of this “rusty carbon sink” in permafrost soils or of how it will respond to changing redox conditions associated with permafrost thaw.

In order to address this knowledge gap, we examined peatland soils collected from three different thaw stages in Stordalen mire (Abisko, Sweden). Following the classification of Johansson *et al* (2006) (19) (Fig. 1), these three thaw stages are: (1) desiccating palsa underlain by permafrost, (2) bog with water-logged active layer underlain by permafrost, and (3) fen, completely water-logged and lacking permafrost. In the desiccating palsa area, the active layer is dry and oxic. As the permafrost thaws, the raised palsas collapse and become inundated, transforming to an ombrotrophic bog with a waterlogged active layer but continuously frozen soil underneath. With continued thawing, the bog areas decrease and minerotrophic fen areas expand with complete water saturation and thus even more reducing conditions than the bog. Permafrost thaw progression through these three thaw stages is, however, not necessarily linear (20).

We took cores from all three thaw stages and analyzed iron-carbon associations in three different layers within the cores defined by geochemical stratification: (1) organic horizon, (2) transition zone and (3) mineral horizon (see Methods). We analyzed the solid phase by selective extractions, extended X-ray absorption fine structure (EXAFS), correlative scanning electron microscopy (SEM) and nanoscale secondary ion mass spectrometry (nanoSIMS). This was complemented by geochemical analysis of the porewater and quantification of Fe(III)-reducing bacteria which play a major role for iron mineral reduction under anoxic conditions.

## Results

### Thaw increases aqueous Fe(II) and dissolved organic carbon

Along the thaw gradient, the aqueous Fe(II) concentrations in the porewater increase from average concentrations of 0.02±0.01 mM in the palsa to maximum concentrations of 1.6±0.3 mM in the fen (Fig. 2). This correlates with an increase in dissolved organic carbon (DOC) from 19.7±0.8 mg/L in the palsa to 102.1±14.1 mg/L in the fen area. In the bog porewater, acetate (0.6±0.1 mM) is measurable in deeper depths, whereas lactate (0.8±0.02 mM) is only found at 7.5 cm (Fig. 2). At the fen site, lactate and acetate are detected throughout the depth profile (0.2±0.1 mM), but an additional increase in acetate (2.3±0.01 mM), propionate (0.8±0.02 mM) and butyrate (0.2±0.01 mM) at 6.5 cm depth is observed (Fig. 2). The appearance of butyrate and propionate in the fen porewater is an indicator for ongoing microbial processes such as fermentation and methanogenesis in the more water-logged and thus more reduced fen soils. This is in line with observations from previous studies (21) that highest methane emissions occur in the fen.

### The abundance of Fe(III)-reducing bacteria increases with thaw

The trend in increasing aqueous Fe(II) and DOC concentrations observed across the thaw gradient closely follows the increase in abundance of Fe(III)-reducing bacteria from $2.40 \times 10^3$ cells per g soil (lower and higher 95% confidence interval $1.46 \times 10^3$ and $3.96 \times 10^3$ cells/g, respectively) in the palsa to $3.11 \times 10^5$ cells per g soil in the fen (lower and higher 95% confidence interval $1.85 \times 10^5$, and $4.78 \times 10^5$ cells/g, respectively). This is suggestive of increased microbially-driven Fe(III) mineral dissolution along the thaw gradient (Fig. 2).

### Reactive iron minerals are dissolved along the thaw gradient

In order to determine whether the observed increases in DOC were related to increased Fe(III) mineral reduction and dissolution, we quantified the amount of organic carbon associated with the reactive iron minerals along the thaw gradient by applying the citrate-dithionite iron reduction method (12, 22). This method simultaneously dissolves all reactive solid iron phases and releases the organic carbon associated with these minerals into solution. The extraction

is performed at circumneutral pH to prevent hydrolysis of organic matter as well as its protonation and re-adsorption onto the remaining solid phases and thus its precipitation. A control experiment was conducted at the same pH with equivalent ionic strength (sodium chloride instead of the reducing agent sodium dithionite). Following Lalonde *et al* (2012), the organic carbon which is released in this control is not associated with the reactive iron minerals and was therefore subtracted from the amount of carbon released from the dithionite-citrate extractions as previously described (12). Additionally, we performed a sodium hydroxylamine-HCl extraction (pH<2) to target the poorly crystalline iron minerals, a sodium pyrophosphate extraction (pH 10) to extract colloidal or OM-chelated iron, and a 6 M HCl extraction to obtain the total extractable Fe of the soil layers (referred to as mg Fe(tot) per g). It should be noted that the total amount of iron per dry weight in the layers is different along the thaw gradient. In the following, only the data from cores Palsa A, Bog C and Fen E are discussed (see Fig. 1), but observed trends are supported by further analyses conducted on cores collected at the same time but stored for a longer period (Palsa B, Bog D, Fen F in Fig. 1), and on triplicate cores from each thaw stage collected during a previous campaign (Figs. S1, S2, S3 and S4).

In the transition zone of the palsa, the reducible iron mineral fraction was 72.9 to 93.9% of the total extractable iron (3.5±0.1 to 9.0±0.3 mg Fe(tot) per g soil; Fig. 3; see also Table S1 and Fig. S5). The amount of reactive iron minerals in the transition zone then decreased to 11.1% of the total extractable iron (18.7±0.7 mg Fe(tot) per g soil) in the bog and to 18.3% of the extractable iron (14.5±0.2 mg Fe(tot) per g soil) in the fen (Fig. 3). In the mineral horizons along the thaw gradient, a loss of the reactive iron minerals was also observed, likely due to more reduced conditions favoring Fe(III) mineral reduction at deeper depths. Reactive iron in the palsa mineral layer was 10.0 to 36.6% of the total extractable iron (8.7±0.3 to 13.5±0.2 mg Fe(tot) per g soil) and declined to 7.5% of the total extractable iron (11.7±0.8 mg Fe(tot) per g soil) in the bog and 9.0 to 10.7% of the total iron (16.3±0.4 to 19.01±0.25 mg Fe(tot) per g soil) in the fen (Fig. 3). This loss of reactive iron in the transition zone and mineral horizon was also

confirmed by the hydroxylamine-HCl extraction and iron speciation by EXAFS (Fig. 3). The abundance of colloidal and/or OM-complexed iron (defined by sodium pyrophosphate extractable iron) also decreased along the thaw gradient, giving way to an increasing relative atom percent-based abundance of Fe-bearing clays. This observation is consistent with increasing aluminum concentrations in the extracts (Fig. S5). The iron content in the organic layer increased from almost no iron in the palsa (0.2±0.02 mg Fe(tot) per g soil, all poorly crystalline) to 4.7±0.01 mg Fe(tot) per g soil (with 43.4% of the total extractable iron being reactive iron) in the organic layer of the fen (Fig. 3). We suggest this is driven by Fe(III) reduction in deeper layers leading to mobilization and upwelling of Fe(II), which might precipitate again close to the water surface by oxidation of Fe(II) by $O_2$, which diffuses from the surface, followed by precipitation as Fe(III) oxyhydroxide minerals.

**Dissolution of reactive iron minerals releases associated organic carbon**

With the decline of reactive iron minerals along the thaw gradient, the mineral-associated carbon was mobilized. Carbon is primarily bound to the reactive iron phases in the transition zone and the mineral horizon of the palsa, as well as in the transition zone of the bog (Fig. 4). 9.9 to 14.8% of the total organic carbon (312.1±0.3 to 354.7±0.04 mg organic carbon per g soil) was released by reductive dissolution of reactive iron minerals in the palsa transition (Fig. 4). In the palsa mineral phase, 18.7 to 20.1% of the total organic carbon (72.7±0.29 to 136.1±0.2 mg organic carbon per g soil) was released. In the transition zone of the bog, 39.4% of the total organic carbon (57.5±0.4 mg organic carbon per g soil) was associated with iron minerals (Fig. 4). However, it should be noted that the total amount of carbon was less in these samples when compared to the palsa transition zone due to total carbon loss along the thaw gradient. Highest total amounts of carbon bound by the reactive iron were therefore found in the palsa transition zone with 41.8±10.8 mg per g soil. This is also supported by the strong spatial association of C with Fe minerals in the fine fraction of this transition zone observed by nanoSIMS analysis, which was not observed in other layers along the thaw gradient (Fig. 4,

Fig. S8). The maximum molar ratio of organic carbon to iron of 1.0, based on the maximal sorption capacity of reactive iron oxides for natural organic matter (23), was exceeded in the palsa transition zone and palsa mineral horizon (9.27±2.16 OC:Fe). This suggests co-precipitation and/or chelation of organic compounds which can generate structures with OC:Fe ratios of 6 to 10, as shown in other studies (23), and are consistent with high sodium pyrophosphate extractable iron values for these palsa layers.

**Discussion**

Carbon binding to reactive iron minerals in the palsa area is consistent with previous observations in permafrost regions of the Qinghai-Tibet Plateau (1) where Fe associated carbon represents, on average, 19.5±12.3% of the total soil carbon pool in the upper 30 cm of permafrost soils throughout the year. Our “space for time” approach reveals, for the first time, how we may expect the dynamics of this rusty carbon sink to respond to progressive climate change. This study suggests that, as soon as the conditions in permafrost peatlands become water-logged, the reactive iron minerals are reduced, probably by Fe(III)-reducing bacteria, and the associated carbon is released into the surrounding porewater, potentially leading to greenhouse gas emissions. More work is needed to elucidate the chemical nature of mobilized organic carbon to determine its lability, but our data suggest that direct chelation or co-precipitation of Fe-C structures play an essential role in carbon protection.

Our findings have far-reaching implications in understanding the carbon cycle after permafrost collapse. Assuming a carbon pool of 191.29 x $10^{15}$ g carbon in the active layer (0-30 cm depth) (3) in northern permafrost regions, we suggest that 13.39 x $10^{15}$ to 38.26 x $10^{15}$ g carbon could potentially be bound to reactive iron in permafrost soils. The lower estimate assumes, based on our data, an average of 7% of total organic carbon is bound to reactive iron in active layers underlain by intact permafrost. The higher estimate assumes a maximum of 20% of total organic carbon is bound to reactive iron, based on our data and Mu *et al* (2016) (1). If this iron-bound carbon was mobilized during thaw and is bioavailable, an equivalent of

2 to 5% of the amount of carbon which is currently present in the atmosphere could be emitted as greenhouse gases from thawing permafrost sites as a consequence of iron(III) mineral reduction. It is therefore crucial to further determine the amount of carbon bound to reactive iron minerals in numerous permafrost environments, and the lability/bioavailability of this carbon following its release in order to better predict future greenhouse gas emissions from thawing permafrost soils and improve the accuracy of existing climate models.

## Materials and Methods

### Site description and sample collection

Stordalen Mire is a peatland 10 km southeast of Abisko in northern Sweden (68 22' N, 19 03' E) (24) which is underlain by quartz-feldspar-rich sedimentary rock (Geological Survey of Sweden). The study site is within the discontinuous permafrost region of northern Scandinavia and consists of three distinct sub-habitats which are common to northern wetlands: (1) a well-drained palsa underlain by permafrost, dominated by ericaceous and woody plants, (2) a bog with variable water table depth and some active thawing, dominated by *Sphagnum* spp. mosses, and (3) a fully-thawed and inundated fen, dominated by sedges such as *Eriophorum angustifolium (19, 20)*. In this study, the three sub-habitats were ordered following a temporal succession of apparent time from “palsa”, to “bog” and “fen” as has been done before (20) following the classification of Johansson *et al* (2006) (19). The palsa and bog areas are underlain by permafrost with a thickness of 10-20 m (25). The active layer, depending on the surface topography, ranges from 0.5-1 m thickness at maximum thaw (25, 26). These three thaw stages cover ~98% of the mire’s non-lake surface (20). A thaw-dependent shift in these habitats was observed from 1970 to 2000 during which palsa regions collapsed and bog and fen areas increased by 17% (27). At the same time, an increase in average annual temperature by 2.5°C between 1913 and 2006 was measured, resulting in an annual mean temperature >0°C during the recent decades (28). The total precipitation also increased during this period of time to an annual average of 306 mm (NORDKLIM, data available at

208 http://www.smhi.se/hfa_coord/nordklim). The expansion of wetlands after permafrost melt is a
209 widespread characteristic of peatlands affected by permafrost thawing (29-32) and the
210 successional shift from palsa to bog and fen areas has been documented in other northern
211 peatlands (31-34).

212 In July 2018, cores were taken in duplicates along a gently collapsing thaw gradient from palsa
213 to bog and fen (Fig. S1). Stordalen mire is a protected area with other ongoing field research,
214 thus the extent of coring is strictly limited due to the risk of accelerating permafrost thaw and/or
215 disturbance to other long-term measurements, especially at sensitive sites like erosion fronts.
216 However, extensive context data (https://polar.se/en/research-in-abisko/research-data/) from
217 the Abisko scientific community is available which ensures representative field sampling of a
218 heterogeneous permafrost area, with cores taken following a transect along the direction of
219 hydrological flow from palsa to bog and fen as described by Olefeldt and Roulet (2012) (35).
220 Given the restrictions in place, it was only possible to collect one core per location with two
221 locations sampled for each thaw stage (see also Fig. S1). A Humax corer of 50 cm length and
222 3-cm-diameter with inner core liners was used. The inner liners were washed three times with
223 80% ethanol, six times with sterile MilliQ water and sealed with sterilized butyl rubber stoppers
224 until coring. Butyl rubber stoppers were boiled three times in deionized water and sterilized at
225 121°C for 20 min in an autoclave. Sharp edges were cut into the end of the coring device to
226 help cut the peat layer. A hammer was used to further sample the active layer. Hammering
227 caused compaction of the cores. Therefore, the recorded depths are not comparable to the
228 initial soil profiles and the data is presented by different layers rather than depth. In the palsa
229 and bog area, cores were taken until the depth of the ground ice. Layers at the bottom of the
230 core which contained predominantly ice were excluded from further analyses. Therefore, the
231 soil investigated in this study represented the seasonally thawed active layer at Stordalen mire,
232 ranging from 30 to 49 cm. The cores were stored vertically at 4°C in the dark. Three cores
233 representing desiccating palsa, bog and fen were processed within 3-4 days (see also Fig.

S1). Due to detailed analysis of the first core set (Palsa A, Bog C and Fen E), additional cores (Palsa B, Bog D and Fen F) from each thaw stage were analyzed after storage for 7 months at 4°C in the dark, which is not ideal, but still could be used to determine if preservation of the carbon by reactive iron was stable over longer time periods (Fig. S1). The long-term stored core Palsa B still showed higher abundance of reactive iron minerals than Bog D and Fen F, but less than Palsa A which could be due to natural variability, long-term storage or because it was taken closer to the collapsing edge (Fig. S2). The cores A to F were compared to triplicate cores previously collected in September 2017 at each thaw stage with a Pürckhauer corer and processed directly after sampling, to show that the trends are representative for the whole mire (Fig. S1). The replicate cores showed the same trends of 6 M HCl extractable iron. Readily extractable Fe (defined by 0.5 M HCl extractable iron) showed similar trends to the sodium dithionite citrate or hydroxylamine HCl extraction for all three thaw stages (Fig. S3). The same trend of total organic carbon along the thaw gradient was observed (Fig S4).

**Porewater sampling and analysis**

The cores were kept in a vertical position during transfer into an anoxic glovebox (100% $N_2$). Three different sections were identified by texture and color changes: (1) an organic horizon on top, (2) a middle transition zone between the organic-rich and mineral-rich layer and (3) a mineral horizon at the bottom (Fig. S1). Rhizon porewater samplers (Rhizosphere research products, Netherlands) with a porous sampling area of 10 cm and 0.15 µm pore size were used to extract porewater from three different depths, resulting in one sample representing each organic horizon, transition zone and mineral horizon. The extracted porewater was analyzed for dissolved Fe (total and Fe(II)), organic carbon (DOC) and fatty acids. The samples were centrifuged for 5 min at 5300 g. For total Fe and Fe(II), the supernatant was acidified in 1 M hydrochloric acid (HCl) and quantified spectrophotometrically in triplicate with the ferrozine assay (36). Dissolved OC was quantified in triplicate with a total organic carbon analyzer (High TOC II, Elementar, Elementar Analysensysteme GmbH, Germany). High performance liquid

chromatography (HPLC; class VP with refractive index detector [RID] 10A and photo-diode array detector SPD-M10A VP detectors; Shimadzu, Japan) was used to determine the fatty acid concentrations.

**Core splitting**

The soil cores were removed from their liners under a $N_2$ atmosphere. Each core was sectioned into an organic horizon of varying thickness (4-10 cm), a transition zone (3-5 cm) and mineral horizon (4-10 cm) (Fig. S1). The transition zone represents the boundary between organic and mineral horizon and was additionally defined due to distinct geochemical conditions in the porewater analysis in the middle of the active layer near the boundary between organic and mineral horizon. Calculated bulk densities as a function of soil organic matter following Bockheim *et al* (2003) (37) were consistent with other studies conducted at Stordalen mire (38) (Palsa A: organic horizon: 0.03±0.01 g/cm$^3$, transition zone: 0.08±0.02 g/cm$^3$, mineral horizon: 0.84±0.26 g/cm$^3$; Bog C: organic horizon 0.08±0.01 g/cm$^3$, transition zone 1.29±0.04 g/cm$^3$ and mineral horizon 1.74±0.01 g/cm$^3$, Fen E: organic horizon 0.21±0.02 g/cm$^3$, transition zone 1.97±0.2 g/cm$^3$ and mineral horizon 1.72±0.01 g/cm$^3$). Sub-samples were homogenized and weighed into 10 mL glass vials and kept frozen at -20°C prior to subsequent analysis.

**Selective extractions**

The soil layers were subjected to several chemical extractions to quantify the different iron phases. The soils were kept frozen prior to analysis, then dried at 20°C under anoxic conditions until no further weight loss was observed (less than 24 hours). 0.3 g dry soil was weighed into a 10 mL glass vial with 6.25 mL extractant and $N_2$ headspace. Prior to use, all glassware was washed with 1 M HCl for 10 min, flushed three times with deionized water and once with MilliQ water. Afterwards glassware was sterilized at 180°C in the oven for 4.5 hours. All samples were centrifuged at room temperature for 10 min at 5300 g. After centrifugation the supernatant

was decanted into another 10 mL glass vial. Each extraction was performed in duplicates for each layer. Throughout the extraction, samples were kept in the dark under anoxic conditions ($N_2$ atmosphere). The extracts were analyzed for Fe and DOC as described above. Additionally, the samples were acidified in 1% (v/v) $HNO_3$ and analyzed in duplicates by MP-AES/ICP-MS to get the total Fe, S, P and Al concentrations (Fig. S5). The illustrated iron values throughout the whole study represent the iron values obtained by the ferrozine assay (for differences in iron concentrations through the different analysis see Fig. S6). Due to dark color of the extracts which can disturb the spectrophotometric measurement during ferrozine complexation, the absorbance of blanks (sample diluted in 1 M HCl or hydroxylamine-HCl) was measured before ferrozine addition and later subtracted to avoid overestimation of iron concentrations. The trends of all Fe analysis (ferrozine assay, MP-AES/ICP-MS analysis) show all the same iron trends with depth and along the thaw gradient (Fig. S6). For additional extractant-specific experimental parameters see below.

*6 M HCl*

To quantify the total extractable Fe of the soil layers, dried samples were subjected to a 70°C 6 M HCl extraction for 24 h (39, 40).

*Sodium pyrophosphate*

The sodium pyrophosphate extraction was performed following Coward *et al* (2017) (10) at pH 10 to determine the colloidal or OM-chelated iron.

*Hydroxylamine-HCl*

To extract the short ranged ordered (SRO) Fe oxides, an acidic hydroxylamine-HCl (pH <2) extraction was carried out under the same conditions as the sodium pyrophosphate extraction (10).

*Dithionite-citrate*

Extractions were conducted using a solution of 0.27 M trisodium citrate, 0.11 M sodium bicarbonate and 0.1 M sodium dithionite (total ionic strength: 1.85 M), as previously described (12). This extraction was used to also quantify the reactive iron minerals but in particular the organic molecules binding to it (released during iron mineral dissolution). Instead of heating to 80°C as described by Lalonde *et al* (2012) (12), the dithionite-citrate extraction was performed under the same conditions as the sodium pyrophosphate and hydroxylamine-HCl extraction (on a rolling shaker at room temperature for 16h) for better comparison between the different extractions. The citrate addition as a metal ion complexing agent was necessary to avoid under-estimation of iron and organic carbon as a result of complexation or mineral precipitation during extraction. Without citrate addition, we obtained 64±3% less iron and 57±28% less carbon after sodium dithionite reductive dissolution. As described in Lalonde *et al* (2012) (12), we also used a 1.85 M sodium chloride/0.11 M sodium bicarbonate extraction as a control experiment under the same conditions (same solid:solution ratio, temperature, time, ionic strength) to distinguish between organic carbon (OC) which is readily desorbed and organic carbon which is released by the reduction of iron(III) minerals. To determine the DOC background concentrations caused by the trisodium citrate, blanks (trisodium citrate sodium bicarbonate solution) were analyzed during each measurement. The background concentration was later subtracted from the total DOC value, as well as the DOC concentration of the control experiment (sodium chloride sodium bicarbonate solution), resulting in the OC which is released by the reduction of reactive iron (see also Fig. S7).

**TOC analysis**

To quantify the total organic carbon (TOC), soil samples from each layer were dried at 60°C until the weight remained constant. The dry soils were then ground and acidified with 16% HCl to remove the inorganic carbon. After washing with deionized water and subsequent drying, the TOC content was analyzed by an Elementar vario El (Elementar Analysensysteme GmbH, Germany). The TOC content goes in line with previously reported values (41).

335 **EXAFS/XANES analysis**

336 Samples were dried under an $N_2$ atmosphere and stored anoxically in a glove box prior to
337 analysis. Sample were then sealed in plastic multi-sample holders with Kapton polyimide tape
338 and kept anoxic until they were transferred to a sample mount at the beamline. The sample
339 holder was in a cryostat during analysis to limit beam damage and to prevent oxidation of
340 Fe(II). Reference samples such as natural nontronite and ferrosmectite (referred to as Fe
341 clays) were obtained from the Clay Mineral Society. Fe(II)-citrate and Fe(III)-citrate were used
342 as reference samples for Fe(II)-OM and Fe(III)-OM, and were prepared and analysed as
343 described in Daugherty *et al* (2017) (42). Mackinawite, used as a reference for FeS, was
344 prepared and analysed as described in Troyer *et al* (2014) (43). 2-line ferrihydrite, prepared
345 and analysed as described in Borch *et al* (2007) (44), was used as a reference for poorly
346 crystalline Fe.

347 Fe K-edge X-ray absorption spectroscopic analyses were conducted at Beamline 11−2 at the
348 Stanford Synchrotron Radiation Light source (SSRL) in Menlo Park, CA. The Si(220) phi = 0°
349 monochromator was used, and beam size of 1 mm vertical and 10 mm horizontal. Iron X-ray
350 absorption near edge structure (XANES) and EXAFS fluorescence spectra were collected with
351 the PIPS detector simultaneously with the transmission spectrum of Fe foil, which was used
352 for internal energy calibrations. Multiple scans (3-4) per sample were acquired as necessary
353 to achieve satisfactory data quality.

354 Scans were calibrated to 7112 eV (the first inflection point of Fe(0), and then averaged over 3
355 or 4 scans using SixPack software. They were deglitched at 7250 and 7600 eV, and then
356 normalized with the E0 value, determined by finding the inflection point of the first derivative of
357 each sample. Linear combination fitting (LCF) of EXAFS spectra was performed in SixPack
358 from chi values of 2 to 12 with an x-weight of 3. Non-negative fits were performed, and
359 components were chosen based on prior knowledge of the sample mineralogy.

## Correlative SEM and nanoSIMS

The two end-members, palsa and fen, were analyzed using SEM and nanoSIMS (see also Figs. S8 and S9) using only the free particles of the fine fraction of the transition zone and the mineral horizon. As described by Kopittke *et al* (2018) (45) and Keiluweit *et al* (2012) (46), subsamples of each layer (1 mg) were dispersed in 10 mL of anoxic deionized water and gently shaken to obtain the free organo-mineral particles from the fine fraction of the soil. 100 µl of the suspension was placed onto a silica wafer and dried under an $N_2$ atmosphere. The samples were sputter-coated with 12 nm platinum (Pt) using a Bal-Tec SCD005 sputter coater.

To characterize the organo-mineral particles of the fine fraction by size and crystallinity and identify representative particles, a field emission scanning electron microscope (FE-SEM; Jeol JSM-6500F), equipped with secondary electron detector, was used prior to nanoSIMS analysis. The acceleration voltage was set to 5 kV, with a working distance of 10 mm.

The nanoSIMS analysis were performed at the Cameca nanoSIMS 50L of the Chair of Soil Science (TU München, Germany). Prior to the measurements, the samples were additionally coated with Au/Pd layer (~30 nm) to avoid charging during the analysis. The $Cs^+$ primary ion beam was used with a primary ion impact energy of 16 keV. Prior to the final measurement, any potential contaminants and the Au/Pd coating layer were sputtered away at 50 x 50 µm with a high primary beam current (pre-sputtering). To enhance the secondary ion yields, $Cs^+$ ions were implanted into the sample during this pre-sputtering process. The primary beam (~1.2 pA) was focused at a lateral resolution ~100 nm and scanned over the sample with $^{12}C^-$, $^{16}O^-$, $^{12}C^{14}N^-$, $^{31}P^-$, $^{32}S^-$, $^{27}Al^{16}O^-$ and $^{56}Fe^{16}O^-$ secondary ions collected using electron multipliers. To compensate for any charging of the non-conductive mineral particles, the electron flood gun was used. All analyses were performed in imaging mode. For every layer, four representative spots were analyzed to obtain a reliable data basis for the spatial distribution of $^{12}C^-$ and $^{56}Fe^{16}O^-$. Ion images of 30 x 30 µm field of view, 30 planes with a dwell

time of 1 ms/pixel, 256 pixels x 256 pixels were recorded. The estimated depth resolution with 16 keV $Cs^+$ ions was 10 nm.

Finally, the nanoSIMS images were analyzed using the Open MIMS Image plugin available within ImageJ (available free-of-charge at, https:// imagej.nih.gov/ij/). All presented images were corrected for the electron multiplier dead time (44 ns), as well as drift corrected, and the planes accumulated. A median filter was applied on all images.

**Most-probable-number (MPN) counts**

Most-probable number (MPN) counts were performed on the soil samples from the different depths of the cores in seven replicates. MPNs were set up in 96-well plates with liquid media for quantification of Fe(III)-reducing bacteria (47, 48). 5 mM sodium acetate, 5 mM sodium lactate and 5 mM 2-line ferrihydrite (chemically synthesized as previously described (48)) were added to the anoxic media (0.6 g/L $KH_2PO_4$, 0.3 g/L $NH_4Cl$, 0.025 g/L$MgSO_4$ x 7 $H_20$, 0.4 g/L $MgCl_2$ x 6 $H_20$, $CaCl_2$ x 2 $H_20$, 22 mM $NaHCO_3$, 1 mL/L trace element according to Widdel et al (1983) (49), 1 mL/L vitamin solution after Widdel & Pfennig (1981) (50) and 1 mL/L selenite/tungstate solution according to Widdel (1980) (51)). To calculate the cell numbers (cells/g soil) from the positive MPN wells, the software program KLEE was used applying confidence limits of Cornish and Fisher (1938) (52) and the bias correction after Salam (1978) (53, 54).

**Acknowledgments**

The authors would like to acknowledge the Abisko Research Station (Abisko, Sweden) for their support during sampling missions. We thank H. Miller (Colorado State University, Fort Collins, United States) for her assistance with EXAFS analysis, G. Harrington and J. Lugmeier (Munich, Germany) for nanoSIMS analysis and E. Stopelli (Zuerich, Switzerland) for ICP-MS measurements. This work was supported by the University of Tübingen (Programme for the Promotion of Junior Researchers grant to C.B) and by the German Academic Scholar

410 Foundation (scholarship to M.P). Use of the Stanford Synchrotron Radiation Lightsource,
411 SLAC National Accelerator Laboratory, is supported by the U.S. Department of Energy, Office
412 of Science, Office of Basic Energy Sciences under Contract No. DE-AC02-76SF00515.

413 **References**

414 1. C. C. Mu *et al.*, Soil organic carbon stabilization by iron in permafrost regions of the Qinghai-
415 Tibet Plateau. *Geophys Res Lett* **43**, 10286-10294 (2016).
416 2. T. I. Eglinton, Geochemistry: A rusty carbon sink. *Nature* **483**, 165-166 (2012).
417 3.. C. Tarnocai *et al.*, Soil organic carbon pools in the northern circumpolar permafrost region.
418 *Global Biogeochem Cy* **23**, GB2023 (2009).
419 4. S. A. Zimov, E. A. G. Schuur, F. S. Chapin, Permafrost and the global carbon budget. *Science*
420 **312**, 1612-1613 (2006).
421 5. E. A. G. Schuur *et al.*, Climate change and the permafrost carbon feedback. *Nature* **520**, 171-
422 179 (2015).
423 6. L. D. Hinzman *et al.*, Trajectory of the Arctic as an integrated system. *Ecol Appl* **23**, 1837-1868
424 (2013).
425 7. R. K. Pachauri *et al.* (2014): Climate Change 2014: Synthesis Report. Contribution of
426 Working Groups I, II and III to the Fifth Assessment Report of the Intergovernmental Panel on
427 Climate Change, Geneva, Switzerland, IPCC, 151 p., ISBN: 978-92-9169-143-2.
428 8. C. Estop-Aragones *et al.*, Limited release of previously-frozen C and increased new peat
429 formation after thaw in permafrost peatlands. *Soil Biol Biochem* **118**, 115-129 (2018).
430 9. M. Shimizu *et al.*, Dissimilatory Reduction and Transformation of Ferrihydrite-Humic Acid
431 Coprecipitates. *Environ Sci Technol* **47**, 13375-13384 (2013).
432 10. E. K. Coward, A. T. Thompson, A. F. Plante, Iron-mediated mineralogical control of organic
433 matter accumulation in tropical soils. *Geoderma* **306**, 206-216 (2017).
434 11. M. Kleber, R. Mikutta, M. S. Torn, R. Jahn, Poorly crystalline mineral phases protect organic
435 matter in acid subsoil horizons. *Eur J Soil Sci* **56**, 717-725 (2005).
436 12. K. Lalonde, A. Mucci, A. Ouellet, Y. Gelinas, Preservation of organic matter in sediments
437 promoted by iron. *Nature* **483**, 198-200 (2012).

13. T. Riedel, D. Zak, H. Biester, T. Dittmar, Iron traps terrestrially derived dissolved organic matter at redox interfaces. *P Natl Acad Sci USA* **110**, 10101-10105 (2013).
14. E. M. Herndon *et al.*, Pathways of anaerobic organic matter decomposition in tundra soils from Barrow, Alaska. *J Geophys Res-Biogeo* **120**, 2345-2359 (2015).
15. D. A. Lipson, M. Jha, T. K. Raab, W. C. Oechel, Reduction of iron (III) and humic substances plays a major role in anaerobic respiration in an Arctic peat soil. *J Geophys Res-Biogeo* **115**, G00I06 (2010).
16. D. Olefeldt, M. R. Turetsky, P. M. Crill, A. D. McGuire, Environmental and physical controls on northern terrestrial methane emissions across permafrost zones. *Global Change Biol* **19**, 589-603 (2013).
17. M. R. Turetsky *et al.*, Short-term response of methane fluxes and methanogen activity to water table and soil warming manipulations in an Alaskan peatland. *J Geophys Res-Biogeo* **113**, G000496 (2008).
18. D. Zona *et al.*, Methane fluxes during the initiation of a large-scale water table manipulation experiment in the Alaskan Arctic tundra. *Global Biogeochem Cy* **23**, GB2013 (2009).
19. T. Johansson *et al.*, Decadal vegetation changes in a northern peatland, greenhouse gas fluxes and net radiative forcing. *Global Change Biol* **12**, 2352-2369 (2006).
20. S. B. Hodgkins *et al.*, Changes in peat chemistry associated with permafrost thaw increase greenhouse gas production. *P Natl Acad Sci USA* **111**, 5819-5824 (2014).
21. C. K. McCalley *et al.*, Methane dynamics regulated by microbial community response to permafrost thaw. *Nature* **514**, 478-481 (2014).
22. O. P. Mehra, M. L. Jackson, Iron oxide removal from soils and clays by a dithionite-citrate system buffered with sodium bicarbonate. *Clays Clay Min.* **7**, 317-327 (1958).
23. R. Wagai, L. M. Mayer, Sorptive stabilization of organic matter in soils by hydrous iron oxides. *Geochim Cosmochim Ac* **71**, 25-35 (2007).
24. R. Mondav *et al.*, Discovery of a novel methanogen prevalent in thawing permafrost. *Nat Commun* **5**, 3212 (2014).
25. H. J. Akerman, M. Johansson, Thawing permafrost and thicker active layers in sub-arctic Sweden. *Permafrost Periglac* **19**, 279-292 (2008).

26. J. Klaminder, K. Yoo, J. Rydberg, R. Giesler, An explorative study of mercury export from a thawing palsa mire. *J Geophys Res-Biogeo* **113**, G000776 (2008).
27. N. Malmer, T. Johansson, M. Olsrud, T. R. Christensen, Vegetation, climatic changes and net carbon sequestration in a North-Scandinavian subarctic mire over 30 years. *Global Change Biol* **11**, 1895-1909 (2005).
28. T. V. Callaghan *et al.*, A new climate era in the sub-Arctic: Accelerating climate changes and multiple impacts. *Geophys Res Lett* **37**, L14705 (2010).
29. M. T. Jorgenson, C. H. Racine, J. C. Walters, T. E. Osterkamp, Permafrost degradation and ecological changes associated with a warming climate in central Alaska. *Climatic Change* **48**, 551-579 (2001).
30. J. A. O'Donnell *et al.*, The Effects of Permafrost Thaw on Soil Hydrologic, Thermal, and Carbon Dynamics in an Alaskan Peatland. *Ecosystems* **15**, 213-229 (2012).
31. S. Payette, A. Delwaide, M. Caccianiga, M. Beauchemin, Accelerated thawing of subarctic peatland permafrost over the last 50 years. *Geophys Res Lett* **31**, GL020358 (2004).
32. D. H. Vitt, L. A. Halsey, S. C. Zoltai, The changing landscape of Canada's western boreal forest: the current dynamics of permafrost. *Can J Forest Res* **30**, 283-287 (2000).
33. W. L. Quinton, M. Hayashi, L. E. Chasmer, Permafrost-thaw-induced land-cover change in the Canadian subarctic: implications for water resources. *Hydrol Process* **25**, 152-158 (2011).
34. S. C. Zoltai, Cyclic Development of Permafrost in the Peatlands of Northwestern Alberta, Canada. *Arctic Alpine Res* **25**, 240-246 (1993).
35. D. Olefeldt, N. T. Roulet, Effects of permafrost and hydrology on the composition and transport of dissolved organic carbon in a subarctic peatland complex. *J Geophys Res-Biogeo* **117**, G01005 (2012).
36. L. L. Stookey, Ferrozine - a New Spectrophotometric Reagent for Iron. *Anal Chem* **42**, 779-781 (1970).
37. J. G. Bockheim, K. M. Hinkel, F. E. Nelson, Predicting carbon storage in tundra soils of arctic Alaska. *Soil Sci Soc Am J* **67**, 948-950 (2003).
38. B. E. Rydén, L. Fors, L. Kostov, Physical properties of the tundra soil-water system at Stordalen, Abisko. *Ecological Bulletins* **30**, 27-54 (1980).

496 39. R. C. Aller, J. E. Mackin, R. T. Cox, Diagenesis of Fe and S in Amazon Inner Shelf Muds -
497 Apparent Dominance of Fe Reduction and Implications for the Genesis of Ironstones. *Cont Shelf*
498 *Res* **6**, 263-289 (1986).
499 40. S. W. Poulton, D. E. Canfield, Development of a sequential extraction procedure for iron:
500 implications for iron partitioning in continentally derived particulates. *Chem Geol* **214**, 209-221
501 (2005).
502 41. M. Lupascu, J. L. Wadham, E. R. C. Hornibrook, R. D. Pancost, Temperature Sensitivity of
503 Methane Production in the Permafrost Active Layer at Stordalen, Sweden: a Comparison with
504 Non-permafrost Northern Wetlands. *Arct Antarct Alp Res* **44**, 469-482 (2012).
505 42. E. E. Daugherty, B. Gilbert, P. S. Nico, T. Borch, Complexation and Redox Buffering of Iron(II)
506 by Dissolved Organic Matter. *Environ Sci Technol* **51**, 11096-11104 (2017).
507 43. L. D. Troyer, Y. Tang, T. Borch, Simultaneous reduction of arsenic(V) and uranium(VI) by
508 mackinawite: role of uranyl arsenate precipitate formation. *Environ Sci Technol* **48**, 14326-
509 14334 (2014).
510 44. T. Borch, Y. Masue, R. K. Kukkadapu, S. Fendorf, Phosphate imposed limitations on biological
511 reduction and alteration of ferrihydrite. *Environ Sci Technol* **41**, 166-172 (2007).
512 45. P. M. Kopittke *et al.*, Nitrogen-rich microbial products provide new organo-mineral associations
513 for the stabilization of soil organic matter. *Global Change Biol* **24**, 1762-1770 (2018).
514 46. M. Keiluweit *et al.*, Nano-scale investigation of the association of microbial nitrogen residues
515 with iron (hydr)oxides in a forest soil O-horizon. *Geochim Cosmochim Ac* **95**, 213-226 (2012).
516 47. E. D. Melton, A. Rudolph, S. Behrens, C. Schmidt, A. Kappler, Influence of Nutrient
517 Concentrations on MPN Quantification and Enrichment of Nitrate-Reducing Fe(II)-Oxidizing and
518 Fe(III)-Reducing Bacteria from Littoral Freshwater Lake Sediments. *Geomicrobiol J* **31**, 788-
519 801 (2014).
520 48. K. L. Straub, A. Kappler, B. Schink, Enrichment and isolation of ferric-iron- and humic-acid-
521 reducing bacteria. *Method Enzymol* **397**, 58-77 (2005).
522 49. F. Widdel, G. W. Kohring, F. Mayer, Studies on Dissimilatory Sulfate-Reducing Bacteria That
523 Decompose Fatty-Acids .3. Characterization of the Filamentous Gliding Desulfonema-Limicola
524 Gen-Nov Sp-Nov, and Desulfonema-Magnum Sp-Nov. *Arch Microbiol* **134**, 286-294 (1983).

50. F. Widdel, N. Pfennig, Studies on Dissimilatory Sulfate-Reducing Bacteria That Decompose Fatty-Acids .1. Isolation of New Sulfate-Reducing Bacteria Enriched with Acetate from Saline Environments - Description of Desulfobacter-Postgatei Gen-Nov, Sp-Nov. *Arch Microbiol* **129**, 395-400 (1981).

51. F. Widdel, Anaerobic degradation of fatty acdis and benzoic acid by newly isolated species sulphate-reducing bacteria. *Dissertation, University Goettingen, FRG* (1980).

52. E. A. F. Cornish, R. A. Fisher, Moments and cumulants in the specification of distributions. *Revue de l'Institut International de Statistique/Rev. Int. Stat. Inst. 5* **4**, 307-320 (1938).

53. A. J. Klee, A Computer-Program for the Determination of Most Probable Number and Its Confidence-Limits. *J Microbiol Meth* **18**, 91-98 (1993).

54. I. A. K. Salama, G. G. Koch, H.D. Tolley, On the estimation of the most probable number in a serial dilution technique. *Commun. Stat. - Theory Methods* **A7**, 1267-1281 (1978).

## Figures and Tables

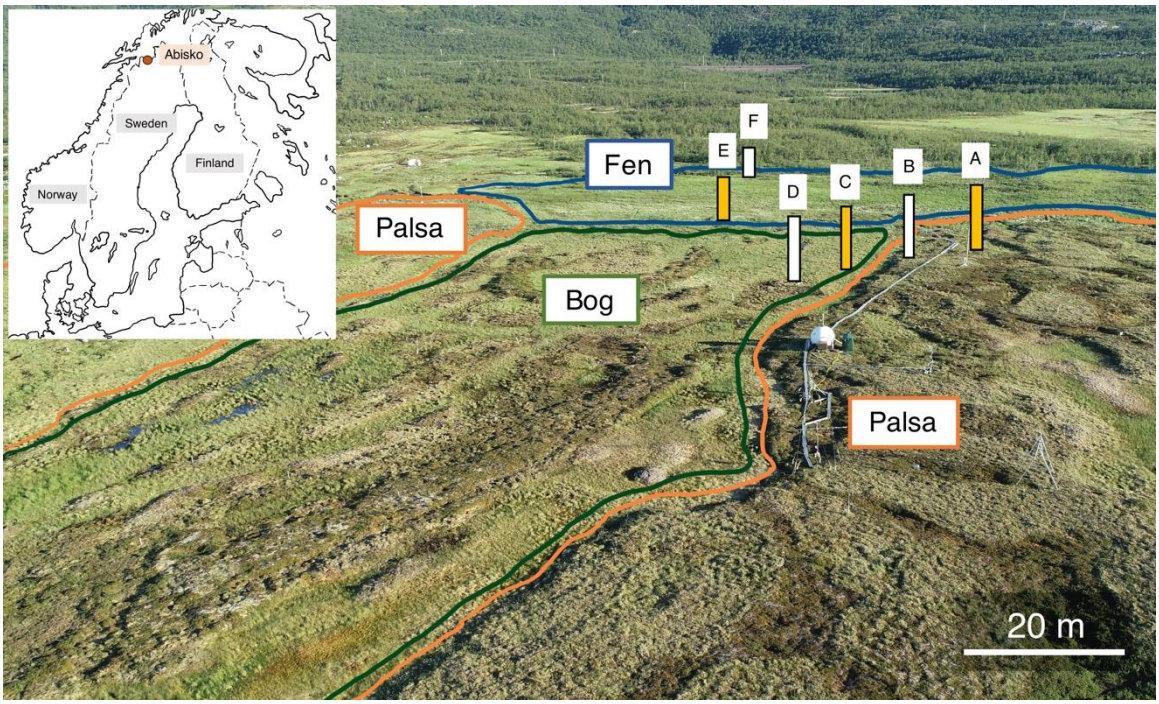


**Fig. 1.** Field site Stordalen mire close to Abisko in the North of Sweden. The three main thaw stages are (1) palsa (marked in orange), (2) bog (in green) and (3) fen (in blue). The positions of the three cores analyzed in detail within 3-4 days of collection, which represent all three thaw stages, are shown in yellow. Additional cores (shown in white) were taken and analyzed after 7 months of incubation at 4°C (Fig. S1).

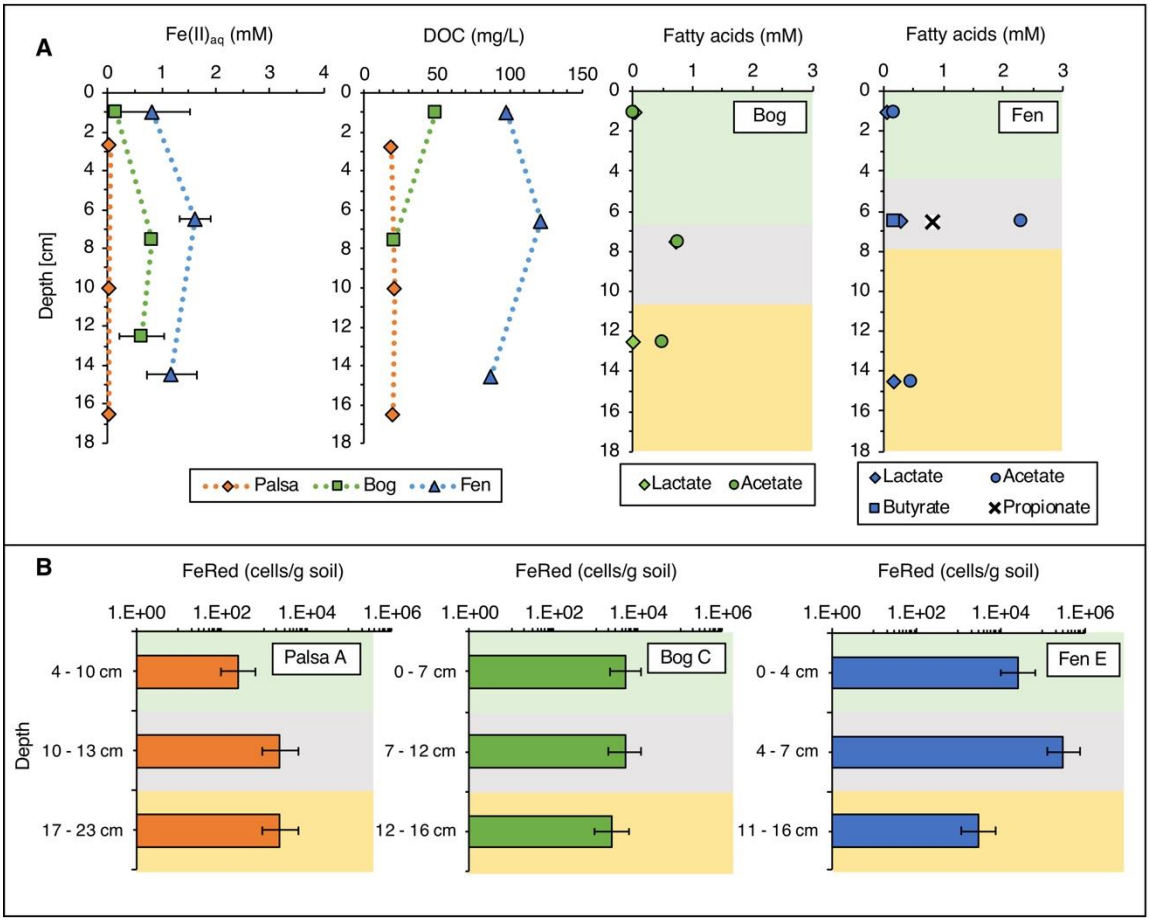


547

548 **Fig. 2.** *(A)* Porewater geochemical analysis of the cores Palsa A, Bog C and Fen E and *(B)*, most
549 probable number quantifications of Fe(III)-reducing bacteria (FeRed) in the solid phase of the cores
550 Palsa A, Bog C and Fen E along the thaw gradient. The error bars of the porewater data represent
551 triplicate measurements. The error bars of the most probable number estimations of Fe(III)-reducers
552 represent 7 replicate analyses and indicate lower and upper limits of the 95% confidence intervals.
553 Please note the differences in the scale of y-axis due to variable thickness of each soil layer along the
554 thaw gradient. The green background marks the organic horizon, grey the transition zone, and yellow
555 the mineral horizon.

556

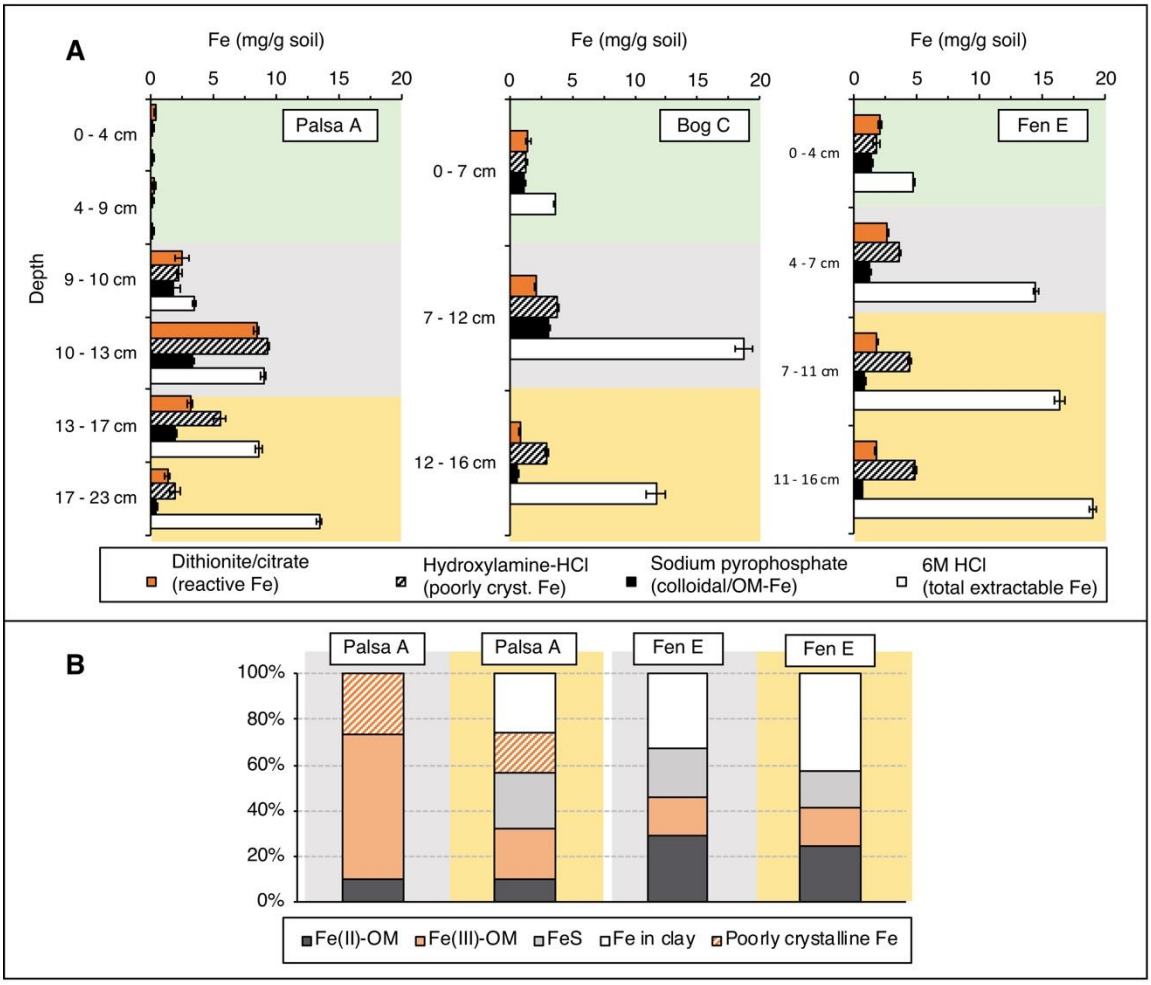


**Fig. 3.** Fe speciation along the thaw gradient determined by *(A)* selective extractions and *(B)* EXAFS. The reactive iron mineral fraction [mg Fe per g soil] was quantified in the different layers and compared to the total extractable Fe (6M HCl extractable Fe, referred to mg Fe(tot) per g soil in the text) and to the colloidal and/or OM-chelated Fe. Please note the differences in the scale of y-axis due to variable thickness of each soil layer along the thaw gradient. The green background marks the organic horizon, grey the transition zone, and yellow the mineral horizon. Error bars represent duplicate extractions of each layer per thaw stage. EXAFS results of the transition zone and the mineral horizon of the two-end members palsa and fen show loss of the poorly crystalline Fe (reference probe: 2-line ferrihydrite), the decrease in OM-chelated Fe (reference probes: Fe(II)-citrate and Fe(III)-citrate), the increase of Fe in clays (reference probes: natural nontronite and ferrosmectite) and Fe sulfur species (reference probe: mackinawite) with depth and along the thaw gradient.

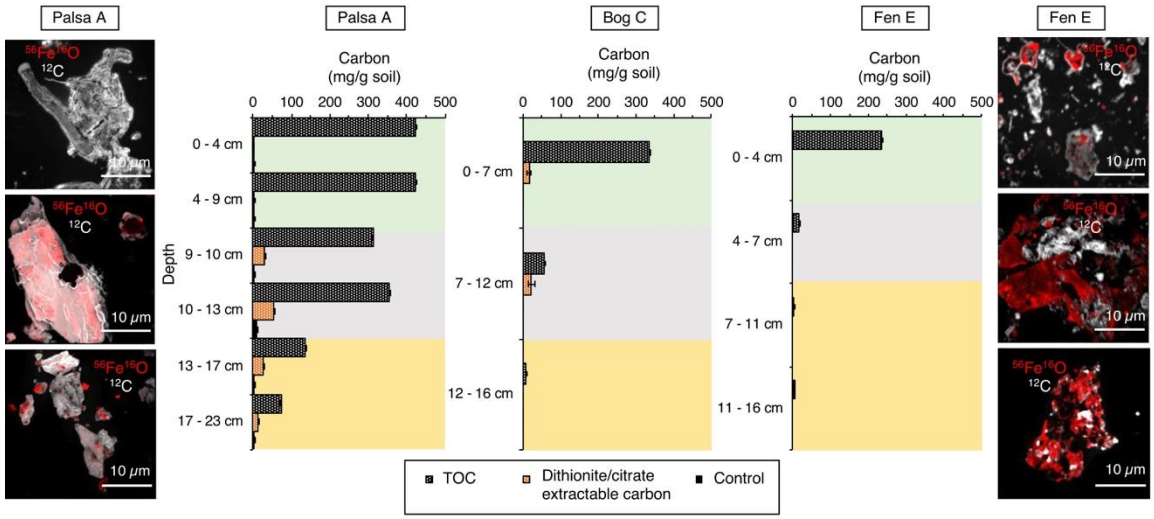


570

571 **Fig. 4.** Left and right: High spatial resolution analysis of iron-carbon associations by nanoSIMS along
572 the thaw gradient (two end-members palsa (left) and fen (right)). The strong spatial association of C to
573 Fe(III) minerals could only be observed in the palsa transition zone. The other fine fractions showed
574 organic-free iron minerals. For the two end-members palsa and fen, four particles of the fine fractions
575 of each layer were analyzed by nanoSIMS, all showing the same spatial distribution of Fe and C as
576 shown by these six representatives (see also Figs. S8 and S9). Middle: Carbon bound by reactive iron
577 minerals along the thaw gradient. The carbon which dislodged from the soil during the reductive
578 dissolution of reactive iron oxides (orange) is shown in comparison to the total organic carbon
579 determined via combustion (black grids, labeled as TOC). The control (same ionic strength and same
580 pH as the sodium dithionite citrate extraction) shows negligible carbon release (Table S1). Errors
581 indicate the range of duplicate analyses of each layer in each thaw stage.

Supplementary Information for

# Iron mineral dissolution during permafrost thaw releases associated organic carbon

**Monique S. Patzner[1], Carsten W. Mueller[2], Miroslava Malusova[1], Verena Nikeleit[1], Thomas Scholten[3], Carmen Hoeschen[2], James M. Byrne[1], Thomas Borch[4], Andreas Kappler[1] & Casey Bryce[1]***

* Casey Bryce

**Email:** casey.bryce@uni-tuebingen.de

582

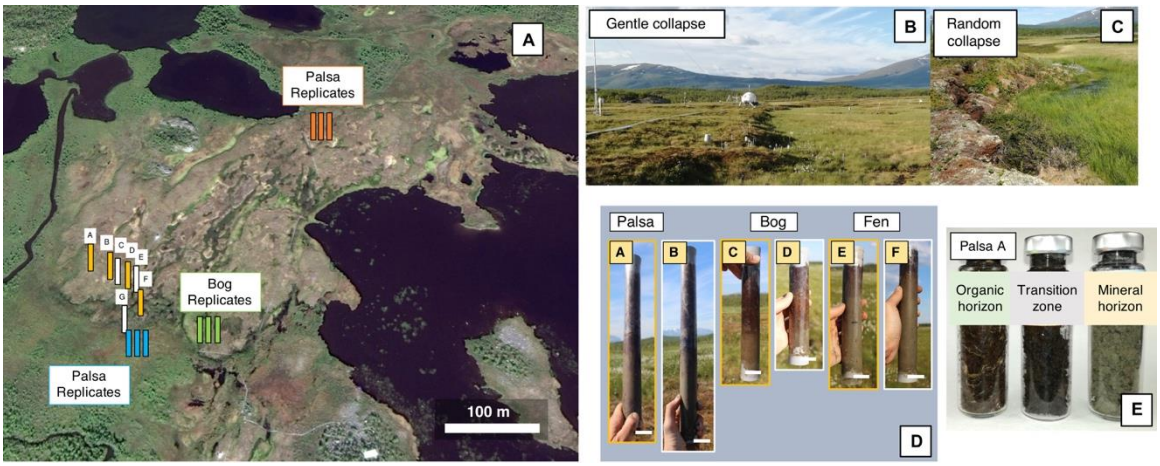


583

584 **Fig. S1.** *(A)* Position of cores taken along a thaw gradient at Stordalen mire (Abisko, Sweden). Cores A
585 to F were taken with a Humax corer and sterile plastic liners in June 2018. Yellow: Cores were
586 immediately split and processed after sampling (3-4 days). White: Cores were stored at 4 °C for 7
587 months and then processed. The data was compared to triplicate cores in each thaw stage (Palsa in
588 orange, Bog in green and Fen in blue) which were taken with a Pürckhauer corer in September 2017
589 and immediately processed after sampling. All cores showed the same trend for total extractable iron,
590 for the poorly crystalline iron and the total carbon along the thaw gradient. *(B)* Gentle collapse of palsa
591 sites at Stordalen mire (Abisko, Sweden). The sampled thaw gradient represents a gentle collapse of
592 palsa to bog and is not randomly collapsing. *(C)* Random collapse of palsa sites at Stordalen mire
593 (Abisko, Sweden). Permafrost thaw does not necessarily progress through all three thaw stages (palsa,
594 bog and fen). Rapid thaw can also create randomly collapsing palsa sites which subsequently become
595 more like a fen. *(D)* Cores taken along a thaw gradient. Palsa: Core A (68°21'18.70"N, 19° 2'38.00"E)
596 and core B (68°21'18.50"N, 19° 2'38.80"E) showed the three main layers in the palsa area: (1) organic
597 horizon, (2) transition zone and (3) mineral horizon. The organic layer was dry and oxic. Bog: Core C
598 (68°21'18.60"N, 19° 2'39.20"E) and core D (68°21'18.30"N, 19° 2'40.00"E) clearly showed the division
599 into the three layers: (1) organic horizon, (2) transition zone and (3) mineral horizon. Both cores were
600 completely water saturated. Fen: Core E (68°21'16.80"N, 19° 2'40.30"E) and core F (68°21'17.80"N,
601 19° 2'41.30"E) also showed the three layers and were water saturated. The cores represent the active
602 layer in July 2018. Yellow: Core A, C and E were immediately split and processed (3-4 days). White:
603 Core C, E and G were stored for 7 months. The Scale bar = 3 cm. *(E)* Example of the subdivision into
604 (1) organic horizon, (2) transition zone and (3) mineral horizon (Palsa A). The cores were split under an
605 $N_2$ atmosphere and immediately frozen in 10 mL glass vials at -20°C till further analysis.

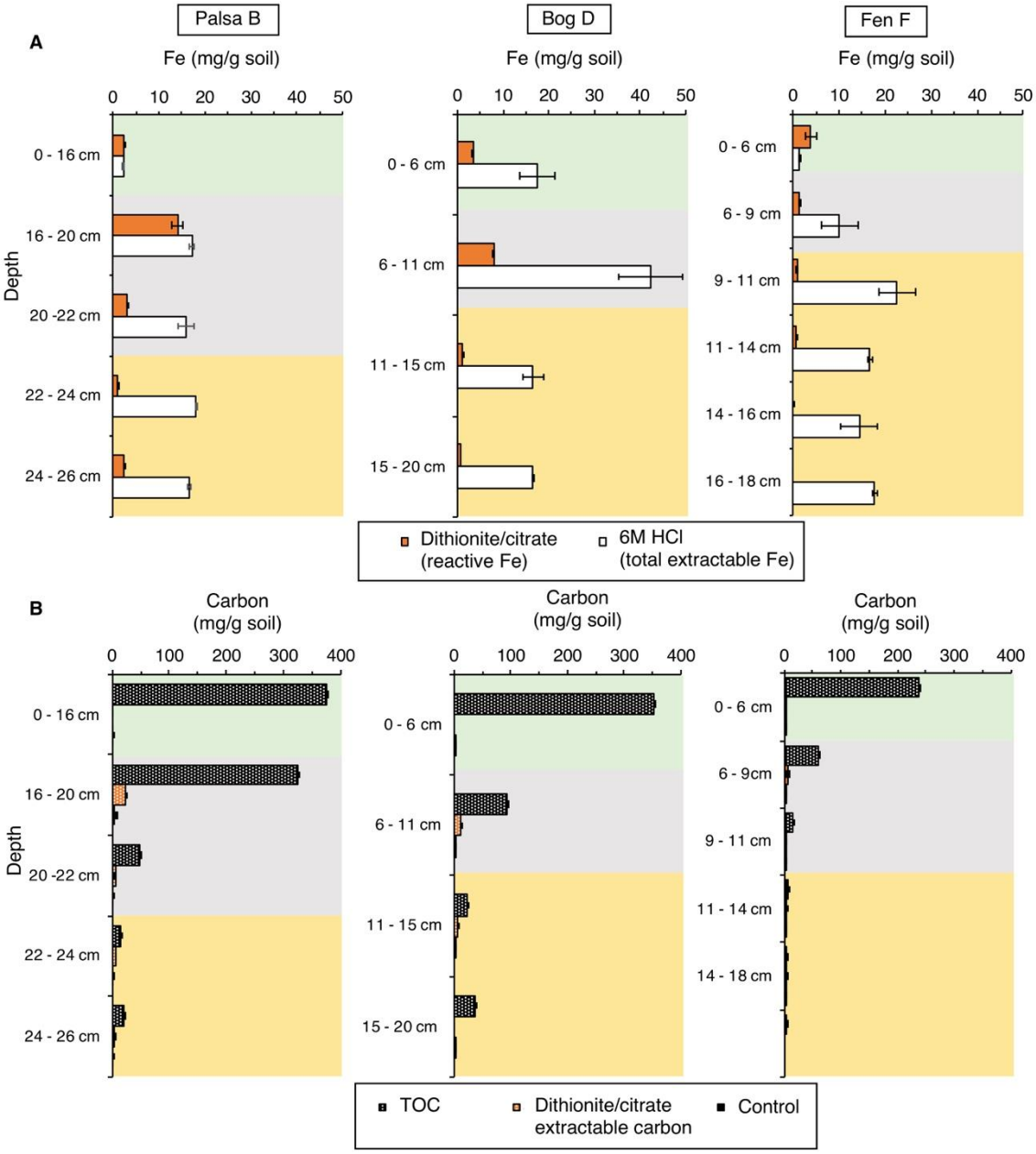


606

607 **Fig. S2.** Extractions of replicate cores. *(A)* Iron and *(B)* carbon concentration of cores Palsa B, Bog D
608 and Fen F. Cores were split after 7 months of incubation at 4°C. The green box marks the organic
609 horizon, grey box the transition zone and yellow box the mineral horizon. Errors indicate the range of
610 duplicate analyses of each layer in each thaw stage. TOC was determined via combustion, whereas the
611 carbon in the dithionite citrate and the control extract (sodium chloride bicarbonate) was determined
612 with the carbon analyzer.

613

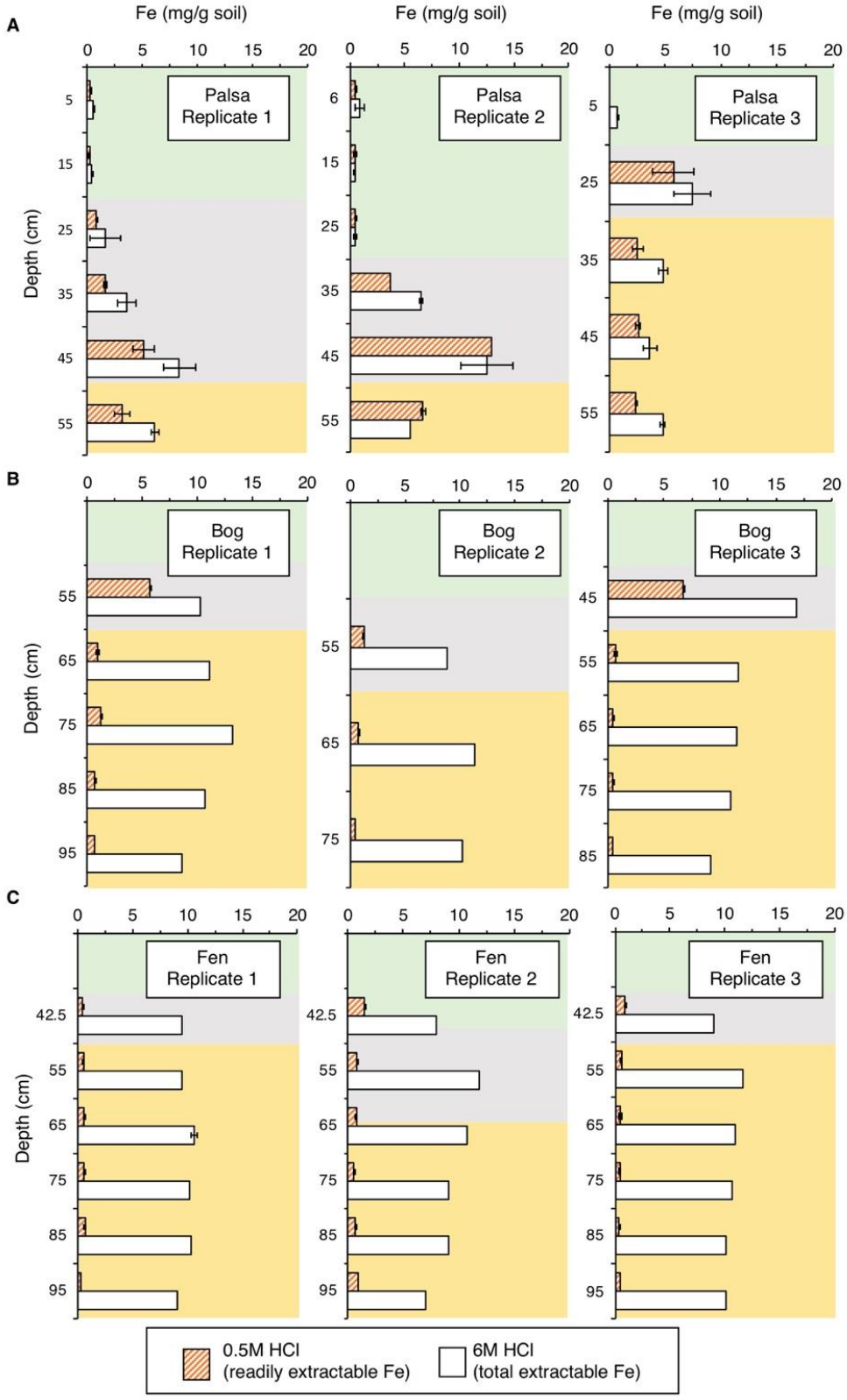


614

615 **Fig. S3.** Iron extractions of replicate cores taken with a Pürckhauer corer: *(A)* Palsa (68°21'26.56"N,

616 19° 3'0.19"E), *(B)* Bog (68°21'16.02"N, 19° 2'49.21"E), (C) Fen (68°21'17.16"N, 19° 2'36.29"E).

Each core was divided into layers in the field and immediately processed. All replicates represent the active layer in September 2017. The bog and the fen soils were waterlogged. The green box marks the organic horizon, grey box the transition zone and yellow box the mineral horizon. Errors indicate the range of duplicate analyses of each layer in each thaw stage.

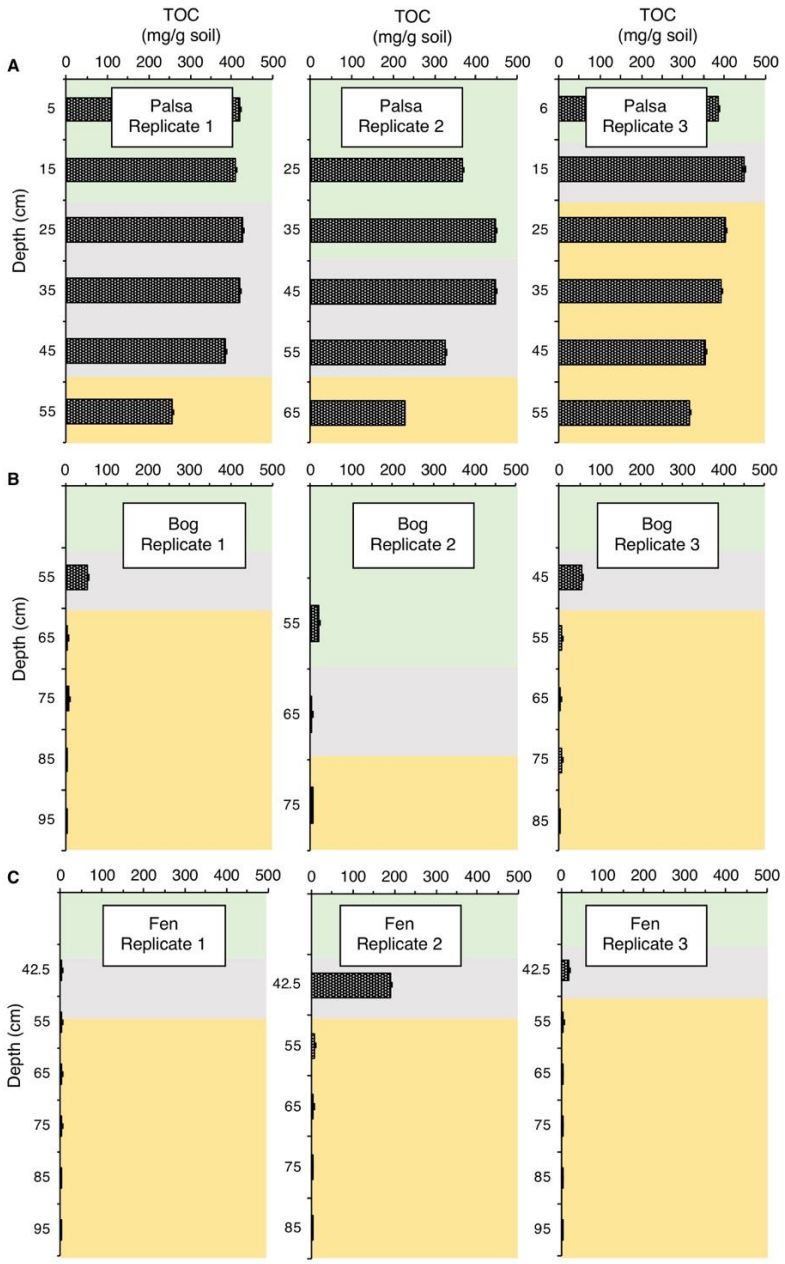


621

622 **Fig. S4.** TOC of replicate cores taken with a Pürckhauer corer: *(A)* Palsa (68°21'26.56"N, 19° 3'0.19"E),
623 *(B)* Bog (68°21'16.02"N, 19° 2'49.21"E) and *(C)* Fen (68°21'17.16"N, 19° 2'36.29"E). Each core was
624 divided into layers in the field and immediately processed. All replicates represent the active layer in
625 September 2017. The bog and fen soils were waterlogged. The green box marks the organic horizon,
626 grey box the transition zone and yellow box the mineral horizon. TOC was determined via combustion.
627 Errors indicate the range of duplicate analyses of each layer in each thaw stage.

628

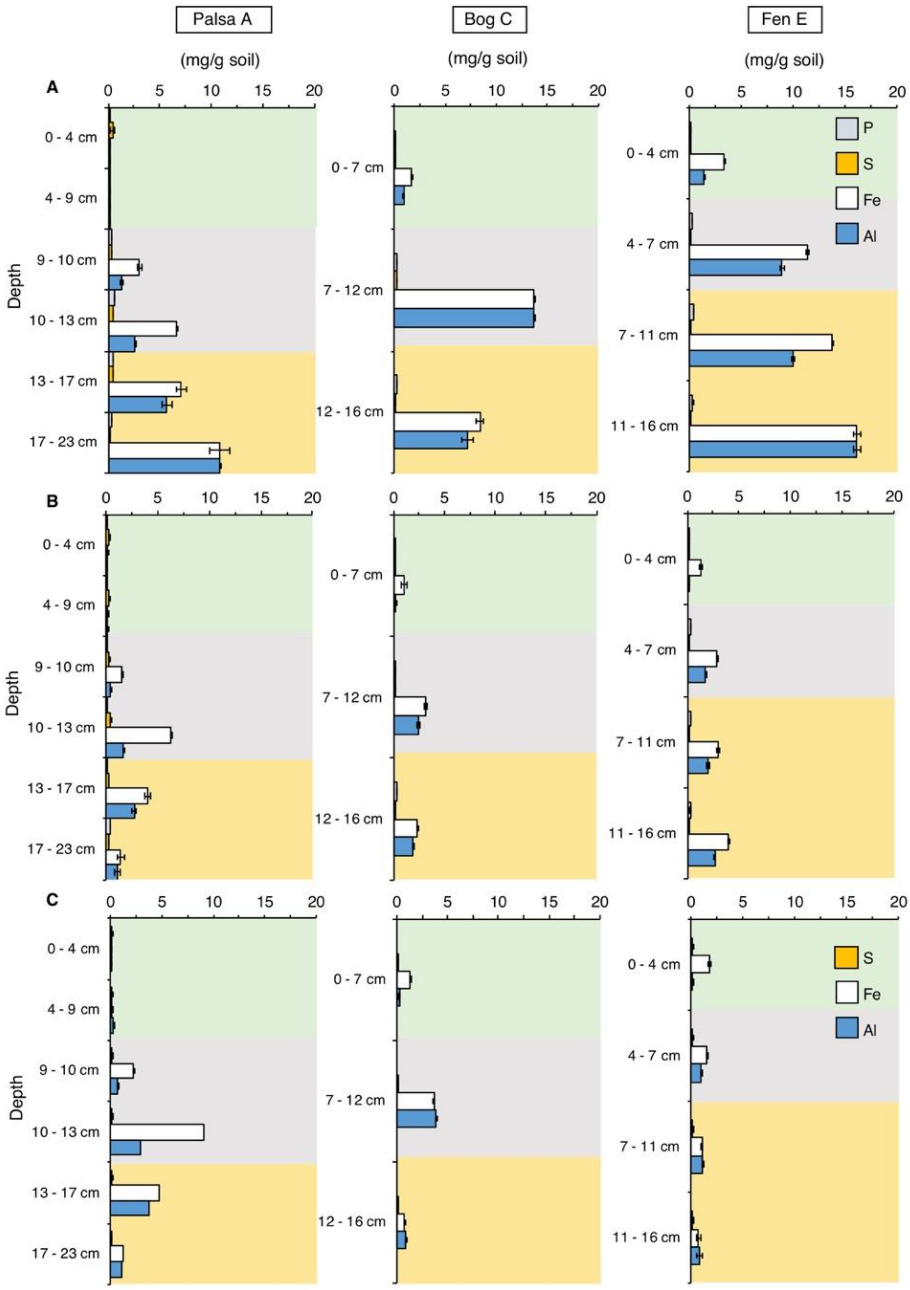


**Fig. S5.** Other elements (P, S, Fe and Al) in extracts of Palsa A, Bog C and Fen E. *(A)* 6M HCl, *(B)* hydroxylamine-HCl and *(C)* Sodium pyrophosphate extracted. Phosphorous (P) and sulphur (S) concentrations were measured with ICP-MS, whereas iron (Fe) and aluminum (Al) concentrations were analyzed using MP-AES. The green box marks the organic horizon, grey box the transition zone and yellow box the mineral horizon. Errors indicate the range of duplicate analyses of each layer in each thaw stage.

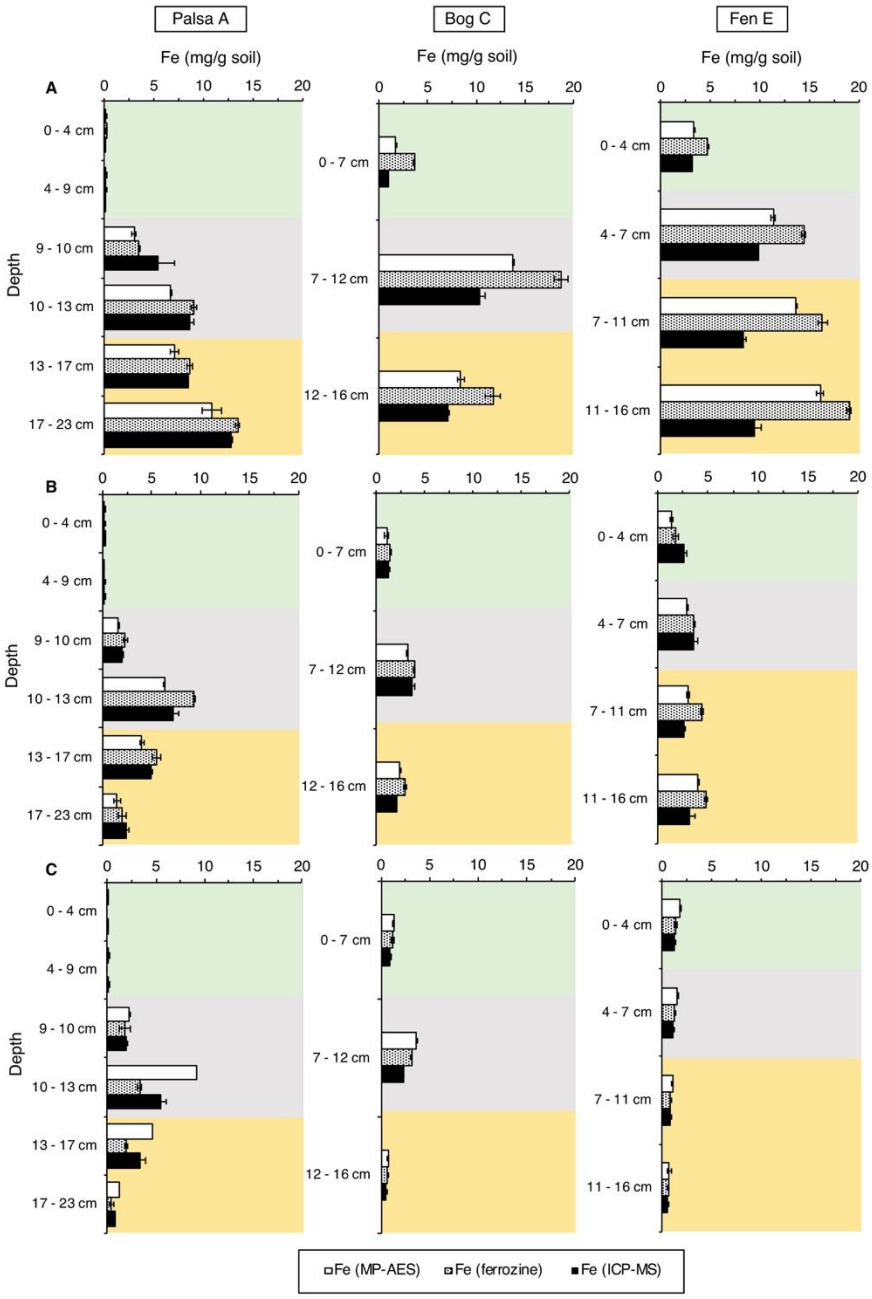


636

637 **Fig. S6.** Fe analysis by MP-AES, ferrozine and ICP-MS analysis. *(A)* 6M HCl extraction. The MP-AES
638 iron values are slightly lower than the ferrozine iron values due to matrix interference during MP-AES
639 measurements of the extracts (HCl). *(B)* Hydroxylamine-HCl extraction. The MP-AES iron values are
640 slightly lower than the ferrozine iron values due to matrix interference during MP-AES measurements of
641 the extracts (HCl). *(C)* Sodium pyrophosphate extraction. The MP-AES values for the sodium
642 pyrophosphate extractable iron are higher than the ferrozine iron values. This could be explained by the
643 dark color of the extracts which disturb the spectrophotometric measurement during ferrozine

644 complexation. After blank subtraction this can result in lower iron concentrations determined by the
645 ferrozine assay.

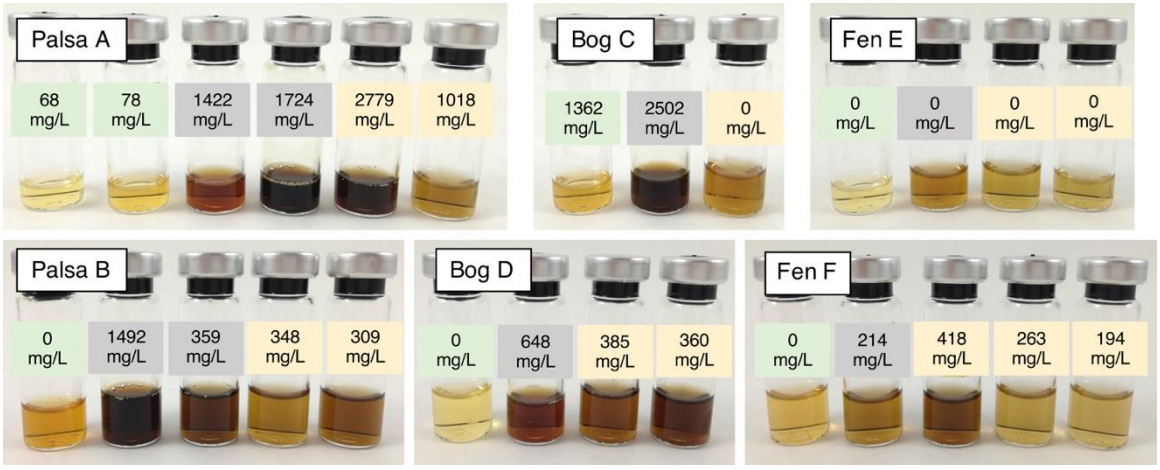


**Fig. S7.** Extracts of sodium dithionite-citrate extraction. Values indicate the dissolved organic carbon concentrations in the extracts after subtraction of the background of the citrate concentration. The background concentration of the citrate for the analysis of Palsa B, Bog D and Fen F was 20.5±0.14 g/L and for the analysis of Palsa C, Bog E and Fen G was 17.8±0.25 g/L. Pictures of the extracts are shown to highlight the loss of the reactive iron phase and carbon associated with it along the thaw gradient, here visible by brown color loss in the extracts from palsa to fen. Green marks the organic horizon, grey the transition zone and yellow the mineral horizon.

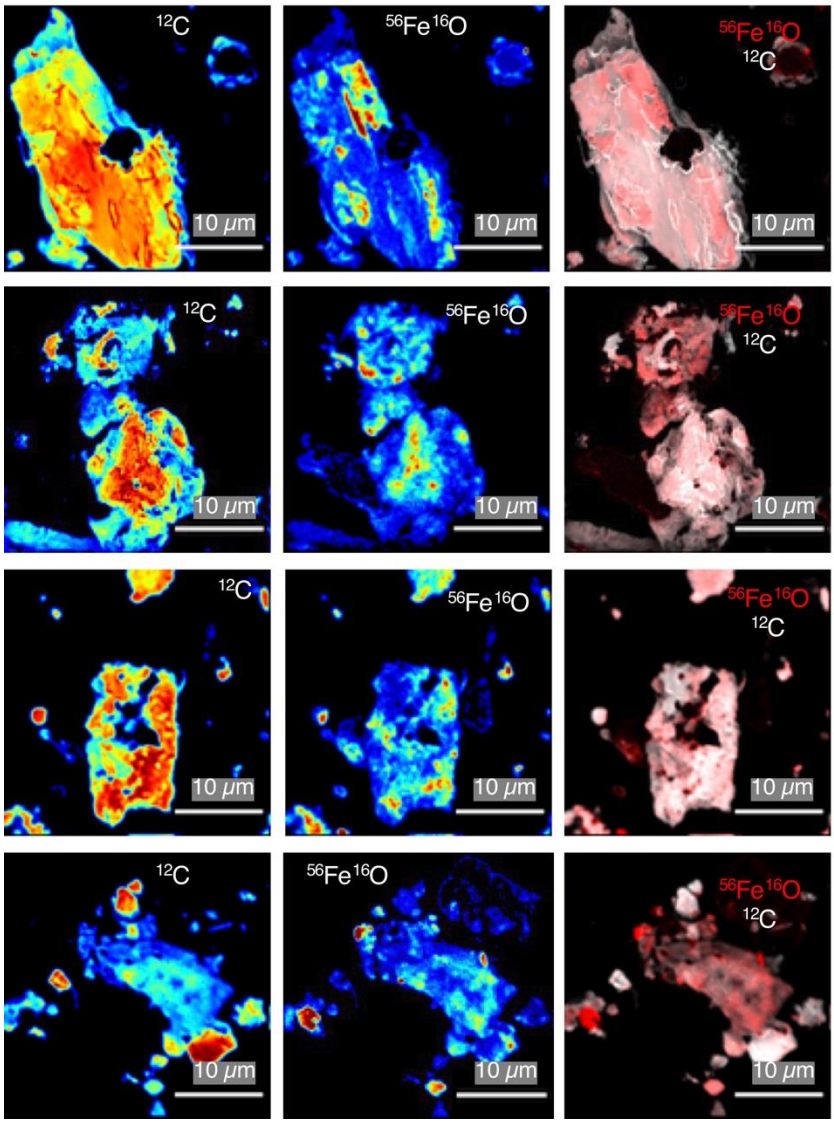


654

655 **Fig. S8.** Four representative particles of the fine fraction of Palsa A analyzed with nanoSIMS showing
656 a close spatial distribution of Fe and C. Seven detectors were used during nanoSIMS measurements
657 for $^{12}C$, $^{56}Fe^{16}O$, $^{16}O$, $^{12}C^{14}N$, $^{31}P$, $^{32}S$ and $^{27}Al^{16}O$. $^{12}C$ and $^{56}Fe^{16}O$ are shown for four representative
658 fine particles plus $^{12}C$ and $^{56}Fe^{16}O$ distributions, overlain in a single image on the left.

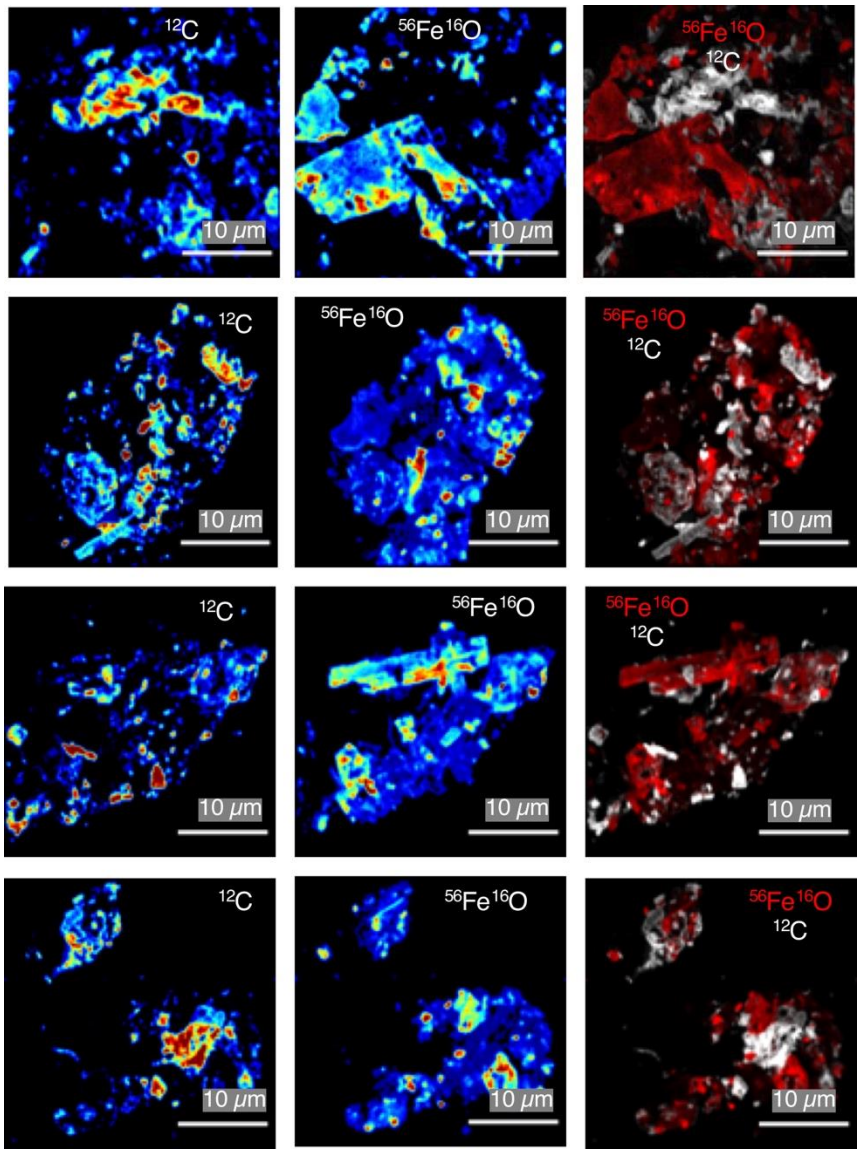


659

660 **Fig. S9.** Four representative particles of the fine fraction of Fen E analyzed with nanoSIMS showing
661 organic-free iron minerals. Seven detectors were used during nanoSIMS measurements for $^{12}C$,
662 $^{56}Fe^{16}O$, $^{16}O$, $^{12}C^{14}N$, $^{31}P$, $^{32}S$ and $^{27}Al^{16}O$. $^{12}C$ and $^{56}Fe^{16}O$ are shown for four representative fine
663 particles plus $^{12}C$ and $^{56}Fe^{16}O$ distributions, overlain in a single image on the left.

664

665 **Table S1.** Absolute and % values of iron and carbon in Palsa B, Bog D and Fen F. In most of the layers,
666 the maximum molar ratio of organic carbon to iron exceeds 1.0, the maximal sorption capacity of reactive
667 iron oxides for natural organic matter (23). Co-precipitation and/or chelation of organic compounds can
668 generate structures with OC:Fe ratios up to 6 to 10 (23). Errors indicate the range of duplicate analyses
669 of each layer in each thaw stage.

| | Reactive iron (control corrected) | Reactive iron of total extractable iron | Control iron | C bound to reactive iron (control corrected) | C bound to reactive iron of the total organic carbon | Control carbon | OC:Fe | Total organic carbon | Total extractable Fe |
|---|---|---|---|---|---|---|---|---|---|
| | mg/g | % | mg/g | mg/g | % | mg/g | | mg/g | mg/g |
| Palsa A | | | | | | | | | |
| Organic horizon | 0.40 ± 0.11 | 100.00 | 0.00 ± 0.00 | 0.94 ± 0.58 | 0.22 | 1.37 ± 0.01 | 2.35 | 423 ± 0.00 | 0.20 ± 0.02 |
| | 0.29 ± 0.09 | 100.00 | 0.00 ± 0.00 | 2.16 ± 0.95 | 0.51 | 1.65 ± 0.08 | 7.45 | 422.91 ± 0.13 | 0.17 ± 0.00 |
| Transition zone | 2.55 ± 0.57 | 72.86 | 0.29 ± 0.08 | 30.99 ± 0.71 | 9.93 | 3.13 ± 0.02 | 12.15 | 312.11 ± 0.33 | 3.51 ± 0.08 |
| | 8.44 ± 0.21 | 93.86 | 0.75 ± 0.11 | 52.50 ± 0.13 | 14.80 | 10.36 ± 0.50 | 6.22 | 354.72 ± 0.04 | 8.99 ± 0.28 |
| Mineral horizon | 3.17 ± 0.19 | 36.58 | 0.25 ± 0.03 | 27.39 ± 1.61 | 20.13 | 2.88 ± 0.08 | 8.64 | 136.11 ± 0.21 | 8.65 ± 0.28 |
| | 1.35 ± 0.21 | 10.00 | 0.07 ± 0.06 | 13.58 ± 0.42 | 18.67 | 1.39 ± 0.10 | 10.06 | 72.71 ± 0.29 | 13.48 ± 0.22 |
| Bog C | | | | | | | | | |
| Organic horizon | 1.48 ± 0.18 | 40.60 | 0.73 ± 0.07 | 16.16 ± 3.91 | 4.85 | 3.16 ± 1.67 | 10.92 | 333.31 ± 0.05 | 3.63 ± 0.05 |
| Transition zone | 2.08 ± 0.05 | 11.14 | 0.41 ± 0.04 | 22.67 ± 8.60 | 39.42 | 1.18 ± 0.21 | 10.90 | 57.51 ± 0.38 | 18.65 ± 0.70 |
| Mineral horizon | 0.88 ± 0.06 | 7.52 | 0.28 ± 0.04 | 0.00 ± 0.00 | 0.00 | 1.04 ± 0.01 | 0.00 | 8.28 ± 0.25 | 11.69 ± 0.81 |
| Fen E | | | | | | | | | |
| Organic horizon | 2.03 ± 0.14 | 43.39 | 0.75 ± 0.00 | 0.00 ± 0.00 | 0.00 | 1.53 ± 0.00 | 0.00 | 234.70 ± 0.83 | 4.68 ± 0.01 |
| Transition zone | 2.64 ± 0.03 | 18.29 | 0.37 ± 0.00 | 0.00 ± 0.00 | 0.00 | 1.38 ± 0.18 | 0.00 | 16.24 ± 0.18 | 14.46 ± 0.22 |
| Mineral horizon | 1.75 ± 0.04 | 10.71 | 0.15 ± 0.00 | 0.00 ± 0.00 | 0.00 | 2.57 ± 0.76 | 0.00 | 3.52 ± 0.05 | 16.34 ± 0.44 |
| | 1.70 ± 0.04 | 8.95 | 0.19 ± 0.01 | 0.00 ± 0.00 | 0.00 | 1.13 ± 0.17 | 0.00 | 4.99 ± 0.10 | 19.01 ± 0.25 |

670